Theoretical and experimental analysis of the von Mises truss subjected to a horizontal load using a new hyperelastic model with hardening

Matteo Pelliciari[a,b], Federico Oyedeji Falope[a,b,*], Luca Lanzoni[a,b], Angelo Marcello Tarantino[a,b]

[a] *DIEF, Department of Engineering "Enzo Ferrari", via Pietro Vivarelli 10, 41125 Modena, Italy*
[b] *CRICT - Centro Interdipartimentale di Ricerca e per i Servizi nel Settore delle Costruzioni, via P. Vivarelli 10, 41125, Modena, Italy*

Abstract

The von Mises truss has been widely studied in the literature because of its numerous applications in multistable and morphing structures. The static equilibrium of this structure was typically addresses by considering only geometric nonlinearities. However, Falope et al. (2021) presented an entirely nonlinear solution in finite elasticity and demonstrated that material nonlinearities play an important role in the prediction of both snap-through and Euler buckling. In such work, the von Mises truss was subjected to a vertical load and thus the system was symmetric and the deformations were relatively small. The present contribution extends the investigation to the case of a horizontal load, which is much more complex due to asymmetry and very large deformations. Since most rubbers employed in technological applications exhibit hardening under large stretches, we propose a new hyperelastic model capable of reproducing this behavior. The advantage of such model compared to the ones available in the literature is that the equilibrium solution maintains a straightforward mathematical form, even when considering compressibility of the material. In addition, in this work we present a new formulation in nonlinear elasticity to predict Euler buckling. The formulation takes into account shear deformation. The analytical prediction agrees well with both finite element (FE) and experimental results, thus demonstrating the accuracy of the proposed model.

Keywords: Truss; Hyperelasticity; Hardening; Euler buckling; Nonlinear elasticity

1. Introduction

Truss structures are used in a wide range of engineering applications. Due to their light weight and cost efficiency, they are especially suitable for long span truss bridges (Catbas et al., 2008), portal trusses

*Corresponding author. Tel.: +39 0592056116.
Email addresses: matteo.pelliciari@unimore.it (Matteo Pelliciari), federicooyedeji.falope@unimore.it (Federico Oyedeji Falope), luca.lanzoni@unimore.it (Luca Lanzoni), angelomarcello.tarantino@unimore.it (Angelo Marcello Tarantino)

for industrial buildings (Haydar et al., 2018), and stadiums (Borri et al., 1992). In the recent years also space structures, such as radars and satellites, have been built using deployable truss structures to keep the devices compact during the launching process (Zhang et al., 2014; Fenci & Currie, 2017).

Truss systems find important applications not only in structural engineering, but also in biomedical sciences. For instance, bone replacements are often performed using custom titanium trusses (Mulhern et al., 2016). Parthasarathy et al. (2011) reported various truss and lattice structures obtained through additive manufacturing to achieve tailored mechanical properties for biomedical applications. Levin (2002) proposed a tensegrity-truss model for the mechanics of the human spine.

The simplest and most studied truss structure is the von Mises (or two-bar) truss (Mises, 1923). Under certain loading conditions, such simple structure exhibits snap-through and bifurcation of the equilibrium (Pecknold et al., 1985). Being a bi-stable system, the von Mises truss is often employed in morphing structures. Barbarino et al. (2013) presented a von Mises truss made of shape memory alloy, which can be heated to activate the snapping from one stable configuration to the other. Chi et al. (2022) discussed the innovative applications of the von Mises truss and other bi-stable systems in soft robotics. Zhang et al. (2021) and Paulose et al. (2015) studied the mechanical response of metastructures consisting of planar arrangements of bi-stable snap-through trusses and beams. Other applications in structures with multiple stable configurations can be found in (Schioler & Pellegrino, 2007; Orlando et al., 2018; Schorr et al., 2018; Chen & Hung, 2011; Chen & Lee, 2021; Wu et al., 2021).

The nonlinear analysis of the static equilibrium of truss structures was always addressed by considering large displacements and small deformations (Bellini, 1972; Ligaro & Valvo, 2006; Kwasniewski, 2009; Cai et al., 2019). Thereby, it was assumed that the material behaves according to a linear elastic constitutive law. This assumption was abandoned in the work by Pelliciari & Tarantino (2020a) and a fully nonlinear formulation for the equilibrium of the von Mises truss was proposed. This theory was then employed for the analysis of more complex truss systems (see, e.g, Fonseca & Gonçalves (2022); Pelliciari & Tarantino (2020b); Silva et al. (2021)), with a particular focus on the prediction of snap-through and bifurcation.

The experimental work by Falope et al. (2021) demonstrated that the analytical model proposed in Pelliciari & Tarantino (2020a) gives an accurate prediction of snap-through and equilibrium path of the von Mises truss subjected to a vertical load. However, in such study, the deformation of the bars is relatively small (maximum compressive strain around 4%). In addition, the system is symmetric and thus both bars undergo the same stress state. Conversely, in the present work we present an analytical, numerical and experimental investigation of the von Mises truss under a horizontal load. In this case the bars reach very

large deformations in both compression and tension. Moreover, the system is asymmetric with one bar under tension and the other one under compression. This makes the study much more complex, especially from the experimental point of view.

Since the deformations involved were relatively small, in Falope et al. (2021) the authors adopted a Mooney-Rivlin (MR) constitutive law. However, this material model is not capable of reproducing hardening that most rubbers exhibit under very large stretches. Therefore, in this work we propose a new refined MR model that reproduces strain hardening in a wide range of deformation. Such a model will be named hardening Mooney-Rivlin (HMR) model. It goes without saying that there are other hyperelastic models for materials with hardening, for instance the Gent model (Gent, 1996), the Ogden-Hill model (Ogden, 1972; Hill, 1979), and the Knowles model (Knowles, 1977)[1]. The above models are especially suitable when the hypothesis of incompressibility is made. Under such hypothesis the solution of the equilibrium of solids under uniaxial tractions (bars of the truss) is straightforward. However, when compressibility is considered, most of such models do not allow to obtain a closed-form solution because the relation between stretch components is not explicit. The main advantage of the hyperelastic law proposed in the present work is that the equilibrium solution maintains its straightforward mathematical form and is derived in closed-form.

The experiments of the present work are carried out using a device designed to avoid Euler buckling of the compressed rod of the truss. In this way, the truss behavior is reproduced and the analytical model is validated. To provide a more comprehensive mechanical investigation, we present additional experiments in which Euler buckling is observed and monitored. Consequently, we propose an analytical formulation for the prediction of Euler instability in nonlinear elasticity.

The prediction of Euler buckling in truss systems gained a lot of attention especially because of the innovative applications of multistable structures. For instance, Guo et al. (2005), Madah & Amir (2017), and Ferrari et al. (2021) studied the optimum design of truss topology under buckling constraints. Bazzucchi et al. (2017) proposed a simple model for Euler instability of the von Mises truss assuming a linear elastic constitutive behavior. Falope et al. (2021) presented a more refined analytical model for the prediction of Euler buckling by including material nonlinearity. In such model, shear deformation was not considered and thus the buckling load was higher than that predicted by a FE analysis. In this work we further improve the model by including shear deformation. We demonstrate that the present formulation is accurate by comparing the buckling loads of first and second mode with experiments and FE predictions.

The paper is organized as follows. In Section 2 we present the analytical model for the equilibrium

[1]For a comprehensive review of hyperelastic models for rubber materials the reader may refer to the work by Horgan (2015).

of the von Mises truss subjected to a horizontal load. The equilibrium is firstly written for a generic hyperelastic isotropic material and then the HMR material model for rubbers with hardening is introduced. The experimental investigation is outlined in Section 3 while the FE analysis is presented in Section 4. The comparison between the results of experimental tests, analytical and FE models is presented in Section 5. In Section 6 and Appendix A we report the study of Euler buckling, which is performed from both experimental and analytical points of view. Finally, conclusions are drawn in Section 7.

2. Analytical model

In this section, we present the analytical formulation for the equilibrium problem of the von Mises truss subjected to a horizontal load. Firstly, the equilibrium equations are derived for a generic hyperelastic isotropic material. Then, the HMR material model for polymers with hardening is presented and the equilibrium equations are specialized to this case.

2.1. Equilibrium of the von Mises truss

The von Mises truss of Figure 1 consists of two equal straight bars connected through a hinge at node C. The bars are composed of an inner deformable material, while the terminal parts are rigid elements. The length of both terminal parts is L_r and it represents the space occupied by the hinge in the experimental device, which is presented in Section 3. The length of the inner deformable part is L_m.

As shown in Figure 1, the apex node C is loaded by the external dead force F, acting in X direction of the global reference system C_1XYZ. Under the effect of the external load, node C undergoes displacements $\hat{u}$ and $\hat{w}$ in X and Z directions respectively. We introduce principal reference systems $x_iy_iz_i$, with $i = 1, 2$. The local components of displacement along axes x_i, y_i and z_i are respectively u_i, v_i and w_i.

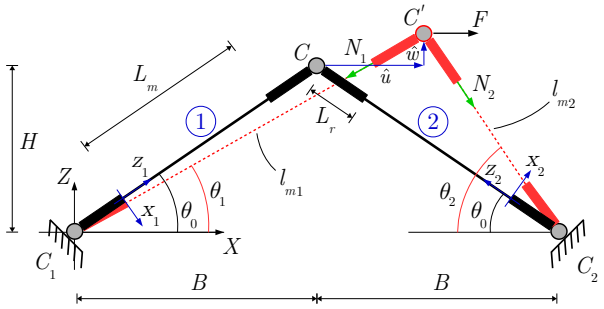

Figure 1: The von Mises truss subjected to a horizontal load F. Each bar is composed of a deformable body with length L_m and two external rigid bodies with length L_r, which represent the space occupied by the hinges in the real structure. After the load application the central hinge C moves to C' with displacement components $\hat{u}$ and $\hat{w}$. Axial forces N_1 and N_2 arise respectively on bars 1 and 2.

The entire length of both bars in reference configuration is $L = \sqrt{B^2 + H^2}$, while in deformed configuration

$$\begin{aligned} l_1 &= \sqrt{(B+\hat{u})^2 + (H+\hat{w})^2}, \\ l_2 &= \sqrt{(B-\hat{u})^2 + (H+\hat{w})^2}. \end{aligned} \tag{1}$$

We indicate with θ_0 the inclination angle of the truss in reference configuration. Angles θ_1 and θ_2 are the inclinations of, respectively, bars 1 and 2 in deformed configuration. The length of the deformable part of the bars in reference configuration is

$$L_m = \sqrt{(B - 2L_r\cos\theta_0)^2 + (H - 2L_r\sin\theta_0)^2}, \tag{2}$$

while in deformed configuration

$$\begin{aligned} l_{m1} &= \sqrt{(B+\hat{u} - 2L_r\cos\theta_1)^2 + (H+\hat{w} - 2L_r\sin\theta_1)^2}, \\ l_{m2} &= \sqrt{(B-\hat{u} - 2L_r\cos\theta_2)^2 + (H+\hat{w} - 2L_r\sin\theta_2)^2}, \end{aligned} \tag{3}$$

where

$$\cos\theta_0 = \frac{B}{L}, \quad \sin\theta_0 = \frac{H}{L}, \quad \cos\theta_1 = \frac{B+\hat{u}}{l_1}, \quad \sin\theta_1 = \frac{H+\hat{w}}{l_1}, \quad \cos\theta_2 = \frac{B-\hat{u}}{l_2}, \quad \sin\theta_2 = \frac{H+\hat{w}}{l_2}. \tag{4}$$

The bars are three-dimensional bodies with a rectangular cross section of width t and height h (t is contained in the XZ plane). It is assumed that the material is homogeneous, isotropic and hyperelastic. The deformation of the bodies is assumed to be homogeneous. Principal stretches $\lambda_{i,j}$ ($i = 1, 2$ and $j = x, y, z$) are introduced, which describe the pure deformation of the bars. Index i indicates the bar while index j indicates the reference axis.

Under the above assumptions, the stored energy function of the i-th bar $\omega_i(I_1, I_2, I_3)$ depends only on the principal invariants of the Cauchy-Green deformation tensor, defined as

$$I_{i,1} = \lambda_{i,x}^2 + \lambda_{i,y}^2 + \lambda_{i,z}^2, \quad I_{i,2} = \lambda_{i,x}^2\lambda_{i,y}^2 + \lambda_{i,x}^2\lambda_{i,z}^2 + \lambda_{i,y}^2\lambda_{i,z}^2, \quad I_{i,3} = \lambda_{i,x}^2\lambda_{i,y}^2\lambda_{i,z}^2. \tag{5}$$

The longitudinal stretches of the bars are computed as

$$\lambda_{i,z} = \frac{l_{mi}}{L_m}, \quad i = 1, 2, \tag{6}$$

where l_{mi} and L_m are given respectively by Eqs. (1) and (2). The equilibrium in the deformed configuration reads

$$\begin{cases} F - N_1\cos\theta_1 + N_2\cos\theta_2 = 0 \\ N_1\sin\theta_1 + N_2\sin\theta_1 = 0 \end{cases} \tag{7}$$

where N_1 and N_2 are the axial stress resultants of bars 1 and 2, respectively.

The body forces are disregarded and the surface tractions generated by the concentrated load F are uniformly and orthogonally distributed on the basis of the bodies. Under such assumptions, the solution of the boundary value problem gives the following relations (Lanzoni & Tarantino, 2015; Pelliciari & Tarantino, 2020a):

$$\lambda_{i,x} = \lambda_{i,y} = \lambda_i = \sqrt{-\frac{\omega_{i,1} + \lambda_{i,z}^2 \omega_{i,2}}{\omega_{i,2} + \lambda_{i,z}^2 \omega_{i,3}}}, \tag{8}$$

$$N_i = -2th\lambda_{i,z} \left(\omega_{i,2}^2 - \omega_{i,1}\omega_{i,3}\right) \frac{\omega_{i,1} + 2\lambda_{i,z}^2 \omega_{i,2} + \lambda_{i,z}^4 \omega_{i,3}}{\left(\omega_{i,2} + \lambda_{i,z}^2 \omega_{i,3}\right)^2}, \tag{9}$$

where $\omega_{i,j} = \partial\omega_i / \partial I_{i,j}$ ($i = 1,2$ and $j = 1,2,3$). By introducing Eqs. (4), (8) and (9) into Eq. (7), the global equilibrium of the von Mises truss assumes the form

$$\begin{cases} F + 2th \left[\dfrac{Q_1}{l_1} (B + \hat{u}) - \dfrac{Q_2}{l_2} (B - \hat{u}) \right] = 0 \\ (H + \hat{w}) \left(\dfrac{Q_1}{l_1} + \dfrac{Q_2}{l_2} \right) = 0 \end{cases} \tag{10}$$

with

$$Q_i = \left(\omega_{i,2}^2 - \omega_{i,1}\omega_{i,3}\right) \frac{\omega_{i,1} + 2\lambda_{i,z}^2 \omega_{i,2} + \lambda_{i,z}^4 \omega_{i,3}}{\left(\omega_{i,2} + \lambda_{i,z}^2 \omega_{i,3}\right)^2}, \quad i = 1,2. \tag{11}$$

The stability of the equilibrium solutions is assessed through the energy criterion (Bažant & Cedolin, 1991; Ziegler, 2013). The total potential energy is defined as

$$\Pi(\hat{u}, \hat{w}) = thL_m \sum_{i=1}^{2} \omega_i - F\hat{u}. \tag{12}$$

The Hessian matrix of the total potential energy is computed as reported in (Pelliciari & Tarantino, 2020a). Stable and unstable equilibrium configurations are distinguished by investigating the sign of the eigenvalues of the Hessian matrix.

2.2. Material model for polymers with hardening

As previously mentioned, the constitutive behavior of the material is defined by a refined compressible MR law in order to include hardening. Firstly, we introduce the MR constitutive law, which is defined by the stored energy function (Ciarlet & Geymonat, 1982)

$$\omega_{\mathrm{MR}}(I_1, I_2, I_3) = a(I_1 - 3) + b(I_2 - 3) + c(I_3 - 1) - (a + 2b + c)\log(I_3), \tag{13}$$

where a, b and c are positive constants. We introduce a hardening function $f(\omega_{\mathrm{MR}})$ and define the following refined constitutive law:

$$\begin{aligned} \omega_{\mathrm{HMR}} &= f(\omega_{\mathrm{MR}})\,\omega_{\mathrm{MR}}, \\ f(\omega_{\mathrm{MR}}) &= 1+\frac{\omega_{\mathrm{MR}}}{2d}, \end{aligned} \tag{14}$$

where d is a positive constant. The limit case when d goes to infinity corresponds to the compressible MR law. As it will be shown, the smaller the value of d the more marked the hardening behavior.

The derivatives of the MR stored energy function (13) with respect to the invariants are

$$\omega_{\mathrm{MR},1}=a, \quad \omega_{\mathrm{MR},2}=b, \quad \omega_{\mathrm{MR},3}=c-\frac{a+2b+c}{I_3}. \tag{15}$$

It follows that the derivatives of the HMR law $(14)_1$ are computed by applying the chain rule

$$\omega_{\mathrm{HMR},j}=\frac{\partial \omega_{\mathrm{HMR}}}{\partial \omega_{\mathrm{MR}}}\omega_{\mathrm{MR},j}=\left(1+\frac{\omega_{\mathrm{MR}}}{d}\right)\omega_{\mathrm{MR},j}, \quad j=1,2,3. \tag{16}$$

The final expression of the equilibrium equations is derived by introducing Eq. (16) into Eq. (10). We remark that, compared to the MR material model, the mathematical form of the equilibrium solution is the same. In fact, the relations between stress and stretch components expressed by Eqs. (8) and (9) remain unchanged.

3. Experimental investigation

In the present section we describe the experimental tests. The specimens were made of rubber so that large deformations were observed. Firstly, uniaxial tests were performed for the material characterization. Then, a device reproducing the von Mises truss was built.

The rubber analyzed in this work is a natural para rubber with hardness value of 45 ShA produced by FIMO (https://www.fimospa.it/Media/Image/Lastre/Elastomeri-compatti.pdf). We characterized the material with uniaxial compression and tensile tests. Three tests were performed on cylindrical and dog-bone specimens by using the machine Instron 5567. We adopted the same geometry and displacement rates as the ones reported in Falope et al. (2021). The experimental curves representing nominal stress vs. stretch are obtained and named S_1, S_2 and S_3. The curves are given in Section 5.1.

After the material characterization, we carried out the experimental test on the von Mises truss. Figure 2 shows the experimental setup of the experimental device. The truss is supported by a steel structure and it is rotated by 90 degrees, so that loads along the direction of gravity reproduce the condition of horizontal loading on the truss.

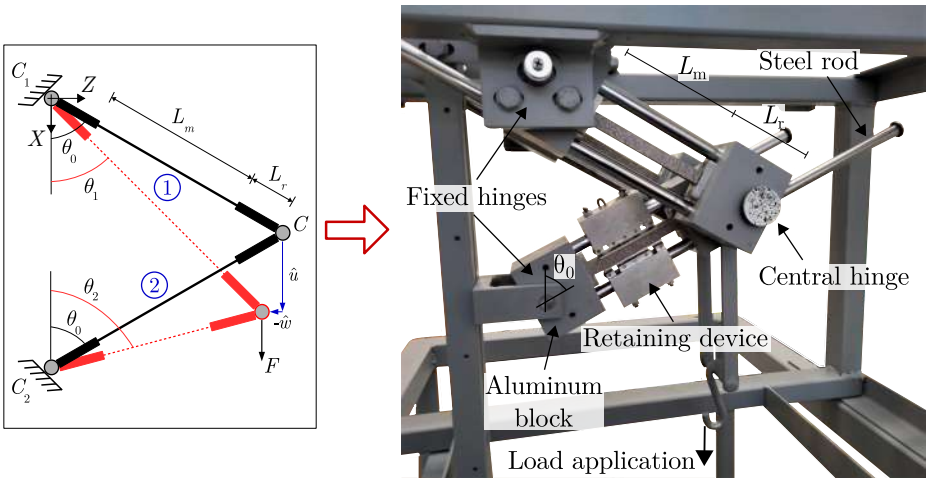

Figure 2: Experimental test on the von Mises truss subjected to a horizontal load. The steel rods keep the terminal faces of the aluminum blocks mutually parallel and slide to avoid relative rotations of the terminal faces of the rubber bars. The retaining device prevents Euler buckling. The load is applied manually by placing weights inside a container and the displacement of central hinge is monitored with DIC technology.

The hinges of the truss are realized with aluminum blocks that rotate freely around the nodes. Fixed hinges C_1 and C_2 are connected to the hinge C through steel rods that avoid relative rotations. The terminal faces of the aluminum blocks are thus forced to remain parallel to one another. The steel rods can slide through circular holes inside the aluminum blocks. This allows the rubber specimen to undergo axial contractions and elongations, reproducing the condition of a sleeve constraint.

A retaining device is introduced to confine bar 2, which is subjected to compression during the experiment. In this way its bending deformation is limited and Euler buckling is prevented. Note that the retaining device does not affect the axial deformation. Bar 1, which is subjected to tensile force throughout the test, is realized with two bars with cross section area $th/2$. The two bars under tension are symmetrically placed with respect to the compressed bar 2. The bar 2 lies in the middle plane of the structure where the load is applied. In this way, torque that would be generated by an eccentric application of the load is avoided. Bars 1 and 2 are not placed in the same plane so that the truss can experience large displacements and reach the alignment of the bars.

Tests were carried out with the geometry of the truss described in Table 1. The load was applied by placing weights inside a container anchored to the hook in Figure 2. The displacement of node C and displacement of the surface of the compressed bar were monitored by means of digital image correlation (DIC)[2].

[2]See Falope et al. (2021) for a detailed description of the DIC set up.

Table 1: Geometry of the von Mises truss for the experimental tests.

Parameter	Value	Unit
θ_0	63	deg
L	182	mm
L_m	90	mm
L_r	46	mm
t	10	mm
h	20.5	mm

4. Finite Element Analysis

In this section we present the FE analysis on the von Mises truss subjected to a horizontal load. Three FE models are built. One reproduces the behavior of the truss by avoiding Euler buckling. The other two models are developed to investigate the response of the structure when Euler buckling takes place.

The FE analysis is carried out using COMSOL Multiphysics® v.6.0. Because of the symmetry with respect to the XZ plane (Figure 1), only half structure is modeled. Namely, only half of height h of the bars is modeled and the vanishing of the displacement normal to the plane of symmetry is imposed. The model is built by coupling the *nonlinear solid mechanics* and *multibody dynamics* modules. The *user defined* hyperelastic material of the FE code is used to assign the MR and HMR laws, expressed respectively by Eqs. (13) and (14).

The hinges of the von Mises truss are modeled by using the feature *rigid attachment* of the nonlinear solid mechanics module and *hinge joint* of the multibody dynamics module. A rigid attachment introduces a rigid cross section, which is then associated with a center of rotation (CoR) by using the hinge joint feature. Figure 3a shows rigid attachments, hinge joints and CoRs defined in the FE models. The attachments assigned to the lower terminal cross sections of the prismatic bars are associated with hinge joints whose CoRs are placed at coordinates $(X = Y = Z = 0)$ and $(X = 2B, Y = Z = 0)$. Conversely, the attachments assigned to the upper terminal cross sections of the prismatic bars are associated with hinge joints characterized by a common CoR placed at the coordinates $(X = B, Y = 0, Z = H)$. These four hinge joints simulate the lower and upper hinges of the truss. For each hinge joint, the rotation of the attachments is constrained around the Y axis.

Buckling of the bars is avoided by introducing *prismatic joints*. This feature constraints two attachments to move along the axis of the prismatic solid. Hence, prismatic joints avoid relative rotations between cross sections reproducing the experimental connection between steel rods and hinge blocks of Figure 2. On bar 1, which undergoes tension under the prescribed positive displacement $\hat{u}$, a single prismatic joint is assigned

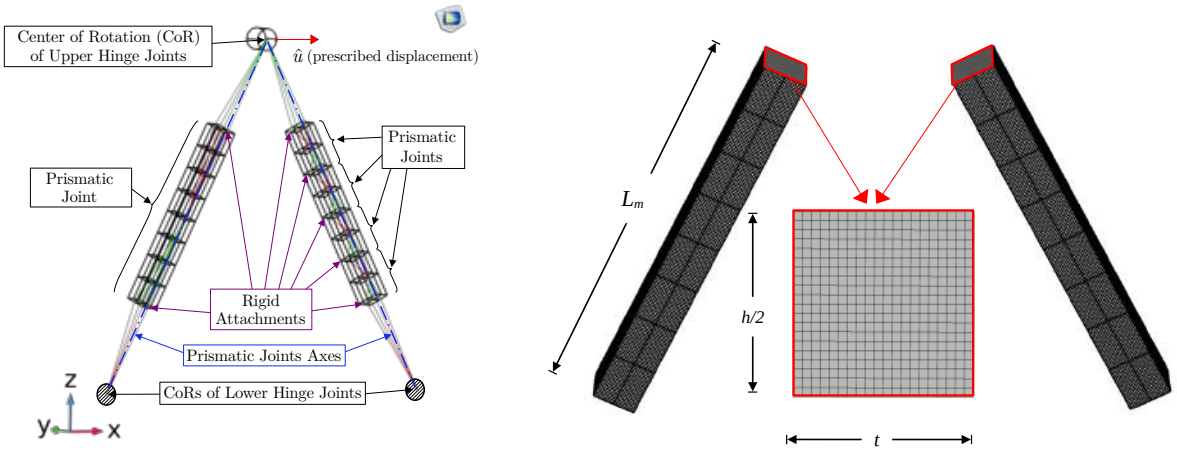

Figure 3: FE model of the von Mises truss built in COMSOL Multiphysics: (a) rigid attachments and hinge joints used to model the hinges of the truss, and prismatic joints introduced to avoid Euler buckling; (b) detail of the mesh.

between the final cross sections of the bar. The axis of this prismatic joint is the longitudinal axis z_1 of bar 1. On bar 2, which undergoes compression under the prescribed positive displacement $\hat{u}$, four equally spaced prismatic joints are introduced (see Figure 3a). The use of four prismatic joints is sufficient to prevent buckling throughout the FE analysis[3].

Three FE models are created with different set up of prismatic joints on bar 2. The FE model 0 is characterized by four prismatic joints, which are depicted in Figure 4a. FE models 1 and 2 are both characterized by only one prismatic joint, with the addition of an external perturbation (see Figs. 4b and 4c). The FE model 0 is used to investigate the behavior of the von Mises truss without bending deformations, while models 1 and 2 are built respectively to observe the first and second buckling modes. The deformed configurations from each model are shown in Figs. 4d-4f [4] .

The FE models are meshed in a way that a mesh independent solution is reached. Each side of the cross section of the bars is subdivided into 20 elements, as shown in Figure 3b. Then, the entire cross section is meshed into 200 rectangular elements with an aspect ratio of 0.98. Finally, the mesh of the cross section is extruded along the length of the solid obtaining cuboid elements with aspect ratio of 0.95. Cubic serendipity shape functions are used for the brick elements.

A static incremental analysis is performed by increasing the values of prescribed displacement $\hat{u}$. The displacement is imposed at the CoR of the upper hinges using the auxiliary sweep of the FE code. The

[3] Appendix A shows that only the first and the second buckling modes can take place during the test. Therefore, it is sufficient to reduce the free length of the bar to $L_m/4$.

[4] The use of a traversal perturbation, namely a small surface pressure at $x_2 = \pm t/2$, allows reaching a buckled solution which is stable from a numerical standpoint.

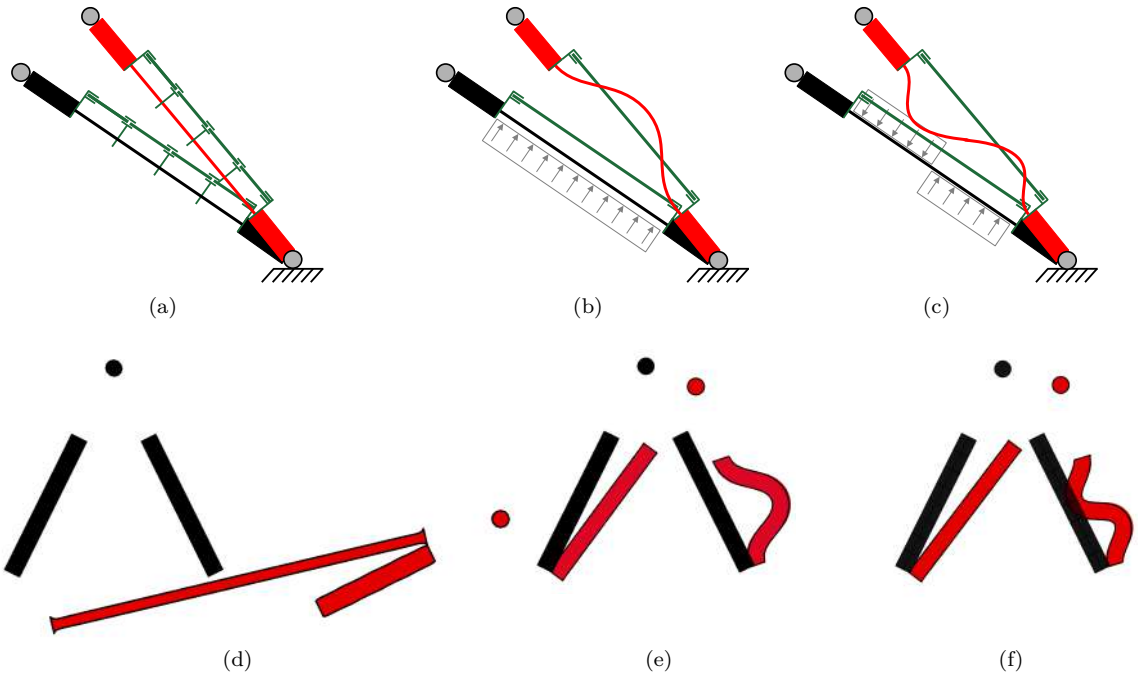

Figure 4: Schematic representation of bar 2 in the FE models and deformed configurations during the analysis: (a) FE model 0 with four prismatic joints that avoid Euler buckling; (b) FE model 1 with a single prismatic joint and application of external perturbation to observe buckling mode 1; (c) FE model 2 with a single prismatic joint and application of external perturbation to observe buckling mode 2; (d), (e) and (f) represent respectively the deformed configurations of models 0, 1 and 2.

incremental analysis goes from displacement 0 to 320 mm with variable increments. The PARDISO solver is employed.

5. Results and discussion

The results from analytical, FE and experimental investigations are reported in the present section. The experimental stress vs. stretch curves of the rubber specimens are presented and the parameters of both MR and HMR constitutive laws are calibrated and discussed. Consequently, the equilibrium paths of the von Mises truss are presented and a comparison between analytical, FE and experimental results is reported. Note that the effect of Euler buckling on the equilibrium of the truss is avoided and it will be discussed in the next section.

5.1. Rubber characterization

The nominal stress vs. stretch curves obtained from the experimental uniaxial tests are shown in Figure 5. The longitudinal stretch of the specimen during the uniaxial test ranges from 0.42 to 4.9. Two gray regions are shown in Figure 5. The one in light gray represents the range of stretch $0.78 \leq \lambda_z \leq 3$, which is the range

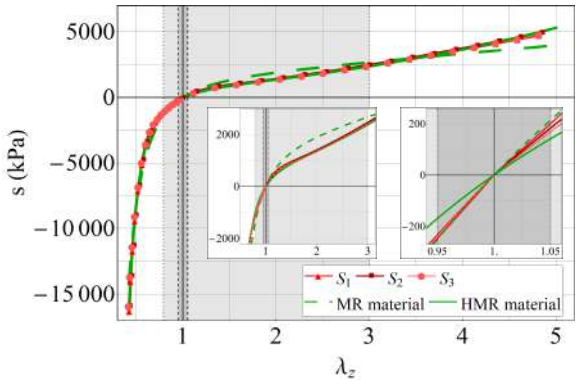

Figure 5: Uniaxial nominal stress vs. stretch curves: experimental data from uniaxial tests on the three specimens S_1, S_2 and S_3 (red curves with markers), analytical curves obtained after calibration of the MR material parameters (dashed green curve) and HMR material parameters (solid green curve). The values of calibrated parameters considered are given in Tabs. 2 and 3.

of deformation tha the two bars of the von Mises truss undergo during the experiment. The region in dark gray ($0.95 \leq \lambda_z \leq 1.05$) shows the behavior in the context of small deformations (linear elasticity).

The constitutive parameters of the MR material (13) and the HMR material (14) are calibrated by fitting the experimental curves S_1, S_2 and S_3 of Figure 5. The parameter vectors of the fitting are $\mathbf{p}_{\text{MR}} = [a,\ b,\ c]$ for the MR material and $\mathbf{p}_{\text{HMR}} = [a,\ b,\ c,\ d]$ for the HMR material. The calibration of the parameters to fit the experimental curves is done in the same way as was done by Falope et al. (2021). In particular, a genetic algorithm is implemented in MATLAB and the following objective function is minimised:

$$\text{obj}(\mathbf{p}) = \sqrt{\frac{\sum_i^n \left[s\left(\lambda_{z_i}, \mathbf{p}\right) - s_i\right]^2}{\sum_i^n s\left(\lambda_{z_i}, \mathbf{p}\right)^2}}, \tag{17}$$

where n is the number of experimental data points, λ_{z_i} and s_i are respectively experimental stretch and stress, $s(\lambda_z,\ \mathbf{p})$ is the fitting function and $\mathbf{p}$ is the parameter vector. Fitting function $s(\lambda_Z,\ \mathbf{p})$ is the nominal stress as a function of the longitudinal stretch, namely N/th computed from Eq. (9).

Two calibrations are performed: one with parameter vector $\mathbf{p}_{\text{MR}}$ and one with parameter vector $\mathbf{p}_{\text{HMR}}$. The optimal values of constitutive parameters are listed in Tabs. 2 and 3. For both analytical and FE investigations, the mean values of the parameters are considered. Tabs. 2 and 3 report also the final values of the objective function for the cases of MR and HMR materials, respectively. We observe that the values of objective function for HMR material are one order less than the corresponding values in case of MR material. This indicates a better accuracy and capability of the HMR to describe the experimental uniaxial response over the entire investigated range of deformation. In fact, the MR law is not capable of capturing hardening of the rubber material analysed, while the HMR gives an accurate description of this behavior.

Const. param.	Experimental curve			Mean± Dev.St
	S_1	S_2	S_3	
a (kPa)	301	320	308	310 ± 9
b (kPa)	482	453	450	461 ± 17
c (kPa)	48913	45445	49926	48095 ± 2350
obj($\mathbf{p}$)	0.131	0.131	0.121	–

Table 2: Optimal values of the constitutive parameters a, b and c of the Mooney-Rivlin (MR) material, obtained from fitting to the uniaxial nominal stress vs. stretch curves S_1, S_2 and S_3.

Const. param.	Experimental curve			Mean± Dev.St
	S_1	S_2	S_3	
a (kPa)	101	110	118	110 ± 9
b (kPa)	410	403	401	405 ± 5
c (kPa)	39321	26347	30259	31976 ± 6655
d (kPa)	2689	2796	3242	2890 ± 293
obj($\mathbf{p}$)	0.0233	0.0202	0.0177	–

Table 3: Optimal values of the constitutive parameters a, b, c and d of the Mooney-Rivlin with hardening (HMR), obtained from fitting to the uniaxial nominal stress vs. stretch curves S_1, S_2 and S_3.

This is clear by looking at the detail on the left in Figure 5.

The detail on the right in Figure 5 shows that the calibrated MR law is more accurate than the HMR law only in the range of small deformations. It goes without saying that this is due to the range of stretch considered for the calibration of parameters. The HMR law comes from an enrichment of the MR law and therefore if the calibration would be performed only for small deformations it would give a more accurate result. However, we are focused on large deformations and thus we are interested in having an accurate prediction of the global response, involving large values of stretch. This is why we calibrated the model parameters considering stretches from 0.4 to 5. The fact that the MR law is more accurate in small deformations is only due to the way we calibrated the material parameters.

The above discussion demonstrated that the proposed HMR law is capable of describing hardening of the rubber analyzed in this work, which is representative of most rubber materials employed in technological applications. However, it is important to stress out the physical meaning of the new parameter d. With this aim, a number of calibrations of the HMR parameter considering different ranges of stretches are carried out. In particular, we consider ranges $1 \leq \lambda_z \leq \lambda_z^{\mathrm{m}}$, with an increasing value of λ_z^{m} ranging from 1.2 to 5 with a step of 0.004. For each range of a calibration is performed and a set of parameters a, b, c and d is estimated. The outcome is shown in Figure 6a.

The parameters are normalized with respect to the following maximum values estimated during the

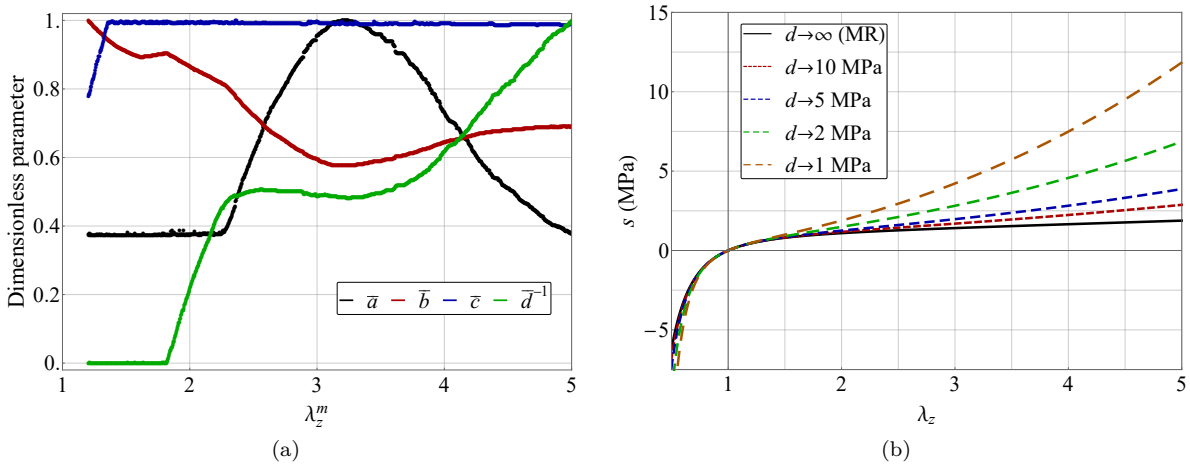

Figure 6: Constitutive parameters of the proposed HMR material model. (a) Dimensionless parameters $\bar{a}$, $\bar{b}$, $\bar{c}$ and $\bar{d}$ obtained from calibrations over ranges of the longitudinal stretch $1 \leq \lambda_z \leq \lambda_z^{\mathrm{m}}$, with λ_z^{m} increasing from 1.2 to 5. The green curve shows that parameter d activates when hardening of the rubber material takes place. (b) Nominal stress vs. stretch curves for different values of hardening parameter d.

calibrations: $a_{\mathrm{m}} = 130$ kPa, $b_{\mathrm{m}} = 680$ kPa, $c_{\mathrm{m}} = 49996$ kPa and ${d_{\mathrm{m}}}^{-1} = 565$ kPa^{-1}. The normalized parameters are indicated with $\bar{a}$, $\bar{b}$, $\bar{c}$ and $\bar{d}$. We recall that when $d \to \infty$ there is no hardening, whereas with decreasing values of d hardening increases. We observe that $\bar{d}^{-1}$ is nearly zero until $\lambda_z^{\mathrm{m}} \approx 1.8$. In fact, the detail on left of Figure 5 shows that the rubber tested in this work exhibits hardening when the longitudinal stretch reaches a value around 1.8. Hence, parameter d activates when hardening behavior of the rubber starts to take place. This gives a direct physical interpretation of the hardening parameter introduced in the present work.

Figure 6b shows the effect of variations of parameter d on the stress-strain response. The values of a, b and c are those reported in Table 3. The curves show that for $d \to \infty$ the response tends to that of the MR law, while as d decreases hardening becomes more pronounced.

5.2. Equilibrium path of the von Mises truss subjected to a horizontal load

The equilibrium path is a three-dimensional curve that shows the trend of the applied horizontal force as a function of horizontal and vertical displacements of the central node C. The analytical equilibrium path is obtained by solving Eq. (10). Two equilibrium paths are computed: one considering the MR material and one using the HMR material. The corresponding values of constitutive parameters are the mean values reported in Tabs. 2 and 3 respectively. The comparison between analytical, experimental and FE equilibrium paths is presented in Figure 7. In detail, the projections of the 3D equilibrium paths on the three coordinated plans are shown in Figs. 7a, 7b and 7c, while the entire 3D path is given in Figure 7d.

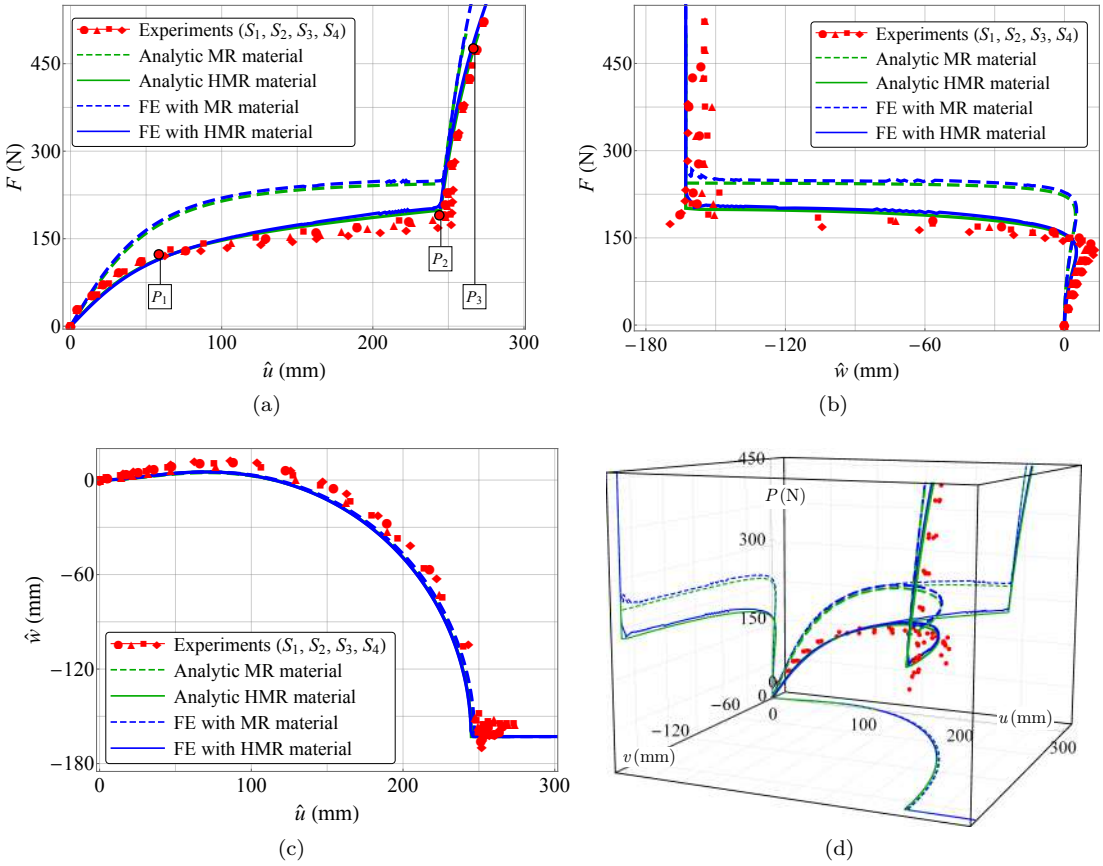

Figure 7: Comparison between equilibrium paths of the von Mises truss subjected to a horizontal load obtained with analytical model (green curves), FE simulation (blue curves) and experimental data (red markers): (a) horizontal force F_x vs. horizontal displacement $\hat{u}$ of the central node; (b) horizontal force F_x vs. vertical displacement $\hat{w}$ of the central node; (c) vertical displacement $\hat{w}$ vs. horizontal displacement $\hat{u}$ of the central node; (d) three-dimensional view of the equilibrium path. The analytical curves are obtained solving Eq. (10) for the cases of MR and HMR materials, with constitutive parameters given in Tabs. 2 and 3 respectively.

There is very good agreement between analytical and FE equilibrium paths for both MR and HMR materials. Comparing with the experimental results, the equilibrium path obtained with HMR material is accurate and gives a good prediction of the experimental behavior. Instead, the one obtained with MR material shows very large errors. This because the MR material is not capable of reproducing accurately the constitutive response of the rubber when subjected to large deformations. Note that, as clear from Figure 7c, in the last part of the experiment the two bars 1 and 2 were aligned. In such condition, the application of loads produced small oscillation around hinges C_1 and C_2. This explains why the final experimental data points in Figs. 7b and 7c are affected by noise.

Figure 8 shows the trend of longitudinal and transversal stretches of the two bars of the truss as a function of horizontal displacement $\hat{u}$. During the application of a monotonically increasing horizontal load,

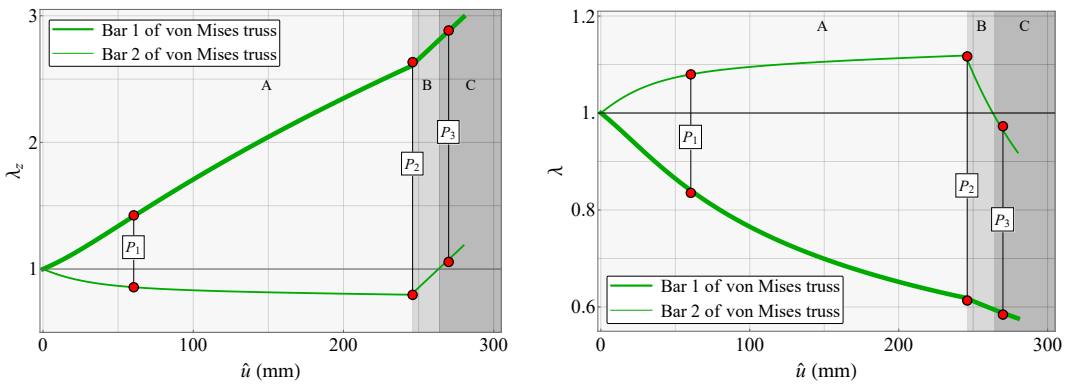

Figure 8: (a) Longitudinal stretch λ_Z and (b) transversal stretch λ of the two bars of the von Mises truss plotted as functions of horizontal displacement $\hat{u}$. The plots are referred to the case of HMR material. Longitudinal and transversal stretches are computed using Eqs. (6) and (8) respectively.

bar 1 is always stretched while bar 2 is compressed until a certain value of $\hat{u}$, after which it starts stretching.

Three characteristic regions are identified and highlighted in Figure 8: region A, where left bar and right bar undergo increasing tensile and compressive states of stress, respectively; region B, in which the bars are horizontally aligned and bar 2 is still under compression but with an unloading phase; region C, where bar 2 switched from a compressive state to a tensile state. The maximum contraction and elongation correspond respectively to longitudinal stretches 0.78 and 3.

Three characteristic points are introduced in Figure 7a: point P_1 lies inside region A and it is associated with displacement $\hat{u} = 60$ mm ($\lambda_{1,z} = 1.42$); point P_2 is placed between region A and region B and is associated with $\hat{u} = 246$ mm ($\lambda_{1,z} = 2.63$); point P_3 is placed inside region C and is associated with $\hat{u} = 270$ mm ($\lambda_{1,z} = 2.88$). Comparing Figs. 8a and 5, it is clearly visible that the uniaxial response of the MR material is not accurate at points P_1 and P_2. In particular, the MR response is stiffer than the experimental one. This is reflected on the global equilibrium path of the von Mises truss shown in Figure 7. The one obtained with MR material is much stiffer and then it tends to approach again the experimental response when point P_3 is reached.

6. Euler buckling analysis

The results presented above were obtained by avoiding Euler buckling of the bar subjected to compression. In this section we focus on the response of the truss when Euler buckling is considered. We present further experiments and an analytical model in nonlinear elasticity to predict Euler instability.

As described in Section 5, the MR material with parameters of Table 2 is accurate for small deformations.

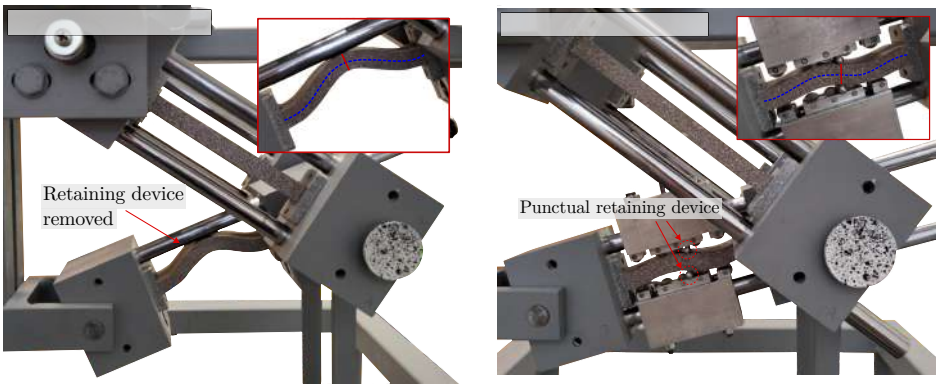

(a) (b)

Figure 9: Experimental tests for the investigation of Euler buckling. (a) The retaining device is removed and thus bar 2 experiences the first buckling mode when the first critical Euler load is reached. (b) A punctual retaining device is applied at the middle cross section of bar 2. The bar experiences the second buckling mode when the second critical Euler load is reached.

Since the bars are composed of a highly deformable material and are relatively slender, we expect that Euler buckling takes place for fairly small loads and deformations. Thus, the prediction of the buckling load will be done by considering the MR material law, which is accurate for this purpose.

The experimental test shown in Figure 7 was performed using retaining devices to avoid Euler buckling. Two additional experiments are carried out in order to observe the first and second buckling modes of the compressed bar (Figure 9). In the first test, the retaining device is removed and thus the bar is free to undergo bending deformation. For this test, the first buckling mode shown in Figure 9a is observed. In the second test, a punctual retaining device is applied at the middle cross section of the bar. Bending deformation is allowed but the first mode is suppressed and therefore the bar experiences the second buckling mode shown in Figure 9b.

The numerical investigation of first and second buckling modes is carried out respectively with FE models 1 and 2, presented in Section 4. The analytical model for Euler instability is outlined in Appendix A. In particular, the critical load path F_{bk}, expressed by Eq. (A.12), is derived. Buckling takes place when F_{bk} intersects the equilibrium path and conditions (A.13) are fulfilled.

The comparison of experimental, analytical and FE predictions of first and second Euler buckling loads is displayed in Figure 10. The green and blue circled crosses indicate respectively analytical and FE predictions of Euler instability. From an experimental point of view it is hard to tell in which step (red dot) buckling takes place. To this regard, in the following we present and discuss the data acquired with DIC during the tests. This allows us to define more clearly when buckling occurs. For now, from Figure 10 we observe that the experimental curves show a slight decrease in stiffness when $\hat{u} \approx 10$ mm and $\hat{u} \approx 20$ mm, for modes 1

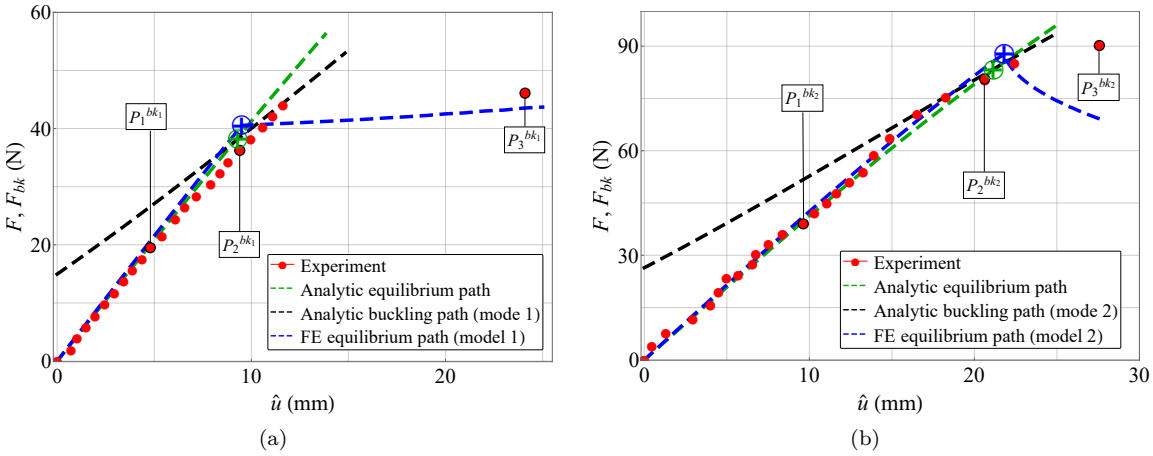

Figure 10: Comparison between experimental data, analytical and FE predictions of (a) first and (b) second Euler buckling loads. The last of the experimental data is the configuration at which the equilibrium of the truss became unstable. The analytical prediction of buckling is given by the green circle, which is the intersection of equilibrium path (green dashed curve) and buckling path (black dashed curve). The buckling in the FE simulation occurs when the FE curve shows an abrupt reduction of stiffness (blue circle).

and 2 respectively. This is already an indication that, near such configurations, buckling starts to take place and affects the equilibrium path.

Three experimental points are selected for each buckling mode. Points $P_1^{bk_1}$ and $P_1^{bk_2}$ are chosen before buckling occurs; points $P_2^{bk_1}$ and $P_2^{bk_2}$ are chosen close to the buckling condition; points $P_3^{bk_1}$ and $P_3^{bk_2}$ are the last experimental data acquired. For each of these points, Figs. 11 and 12 show the contour map of the displacement field acquired with DIC.

Figures 11(b)-(d) show contour plots of the local transversal displacement u_2 during the test for the first buckling mode, which arises due to bending of the specimen. At step $P_1^{bk_1}$ displacement u_2 reaches a maximum value of 0.19 mm. This value is considered negligible and it is due to imperfections, because it is in the order of $0.02t$ (being t the thickness of the bar). Hence, in this step Euler buckling is still not observed. At step $P_2^{bk_1}$ displacement u_2 reaches a maximum value of 0.6 mm, which is in the order of $0.1t$. We identify this displacement value as a threshold for buckling and thus, at this step, Euler instability takes place. Indeed, as shown in Figure 10a, the stiffness of the load path displays a decrease due to bending. At step $P_3^{bk_1}$ the bending deformation is very pronounced. The compressed bar already buckled and the equilibrium loses its stability.

Figures 12(b)-(c) show contour plots of the local transversal displacement u_2 during the test for the second buckling mode. At step $P_1^{bk_2}$ the contour plot starts to show the shape of the second buckling mode. However, the maximum relative displacement is $\Delta u_2 = 0.48$ mm, which is still negligible being in the order

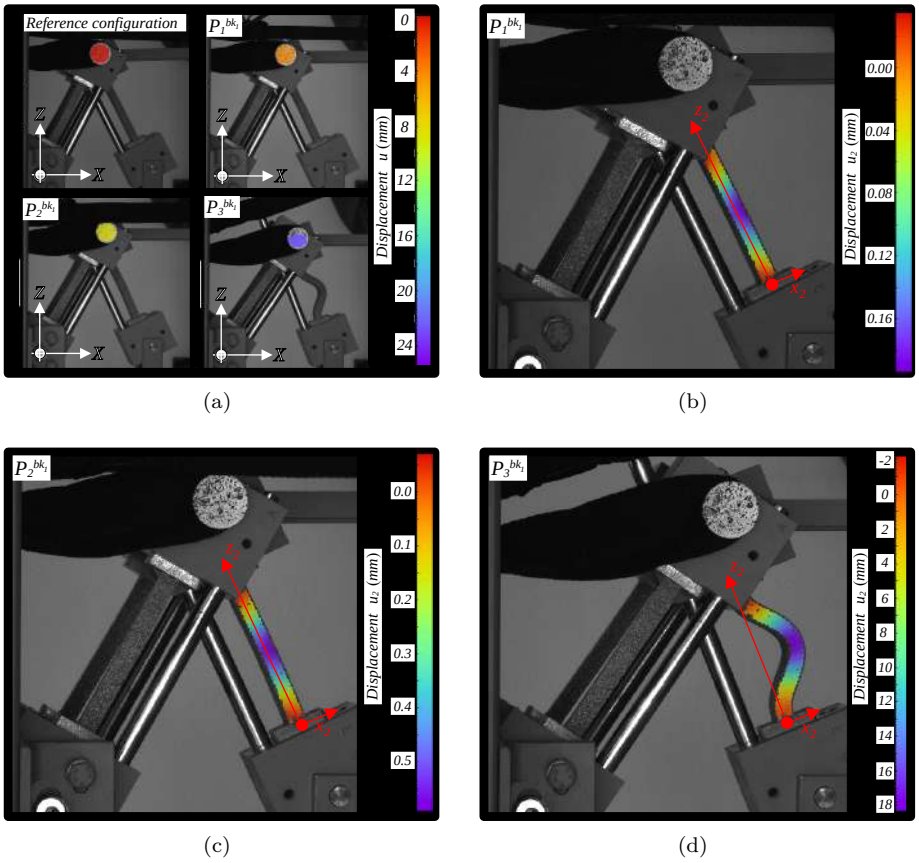

Figure 11: Contour plots of the displacement field from DIC during the experimental test for the first buckling mode: (a) global displacement $\hat{u}$ of the central node at the reference configuration and at steps $P_1^{bk_1}$, $P_2^{bk_1}$ and $P_3^{bk_1}$; (b) local transversal displacement u_2 of bar 2 at step $P_1^{bk_1}$; (c) local displacement u_2 of bar 2 at step $P_2^{bk_1}$; (d) local displacement u_2 of bar 2 at step $P_2^{bk_1}$.

of $0.04t$. At step $P_2^{bk_2}$ the maximum relative displacement is $\Delta u_2 = 1.95$ mm, which is in the order of $0.19t$. The buckling threshold is exceeded and thus Euler instability occurs. At step $P_3^{bk_2}$ the bending deformation of the second buckling mode is pronounced and the compressed bar already buckled.

Figure 13a shows the maximum values of the relative transversal displacement in bar 2 during the tests, plotted as a function of displacement $\hat{u}$ of the central hinge. The red and magenta curves come respectively from the experiments for buckling modes 1 and 2. Initially, in both experiments the displacement increases slightly and buckling is still not observed. As it should be, the two set of experimental data show the same trend. However, near point $P_2^{bk_1}$, the growth rate of transversal displacement in the first test increases relevantly. This is clear from Figure 13b, where we identify a red zone in which buckling mode 1 takes place. The data of the second test are shown in detail in Figure 13c. Also in this case, in the magenta zone the growth rate of transversal displacement increases rapidly and this means that Euler buckling occurs inside

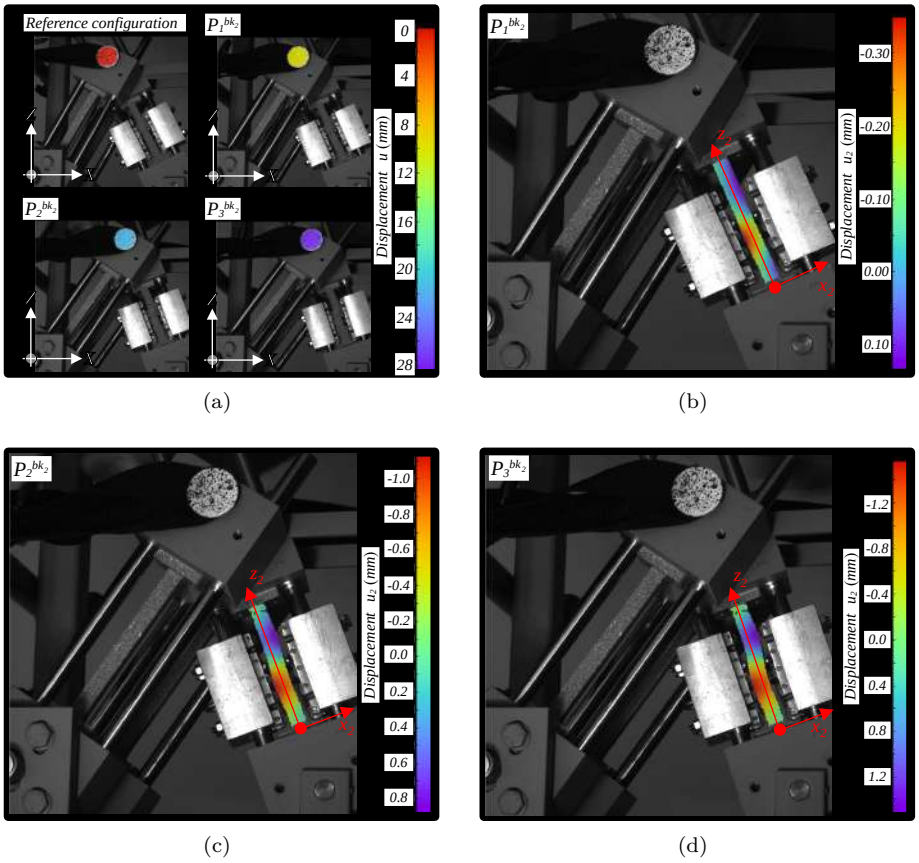

(a) (b)

(c) (d)

Figure 12: Contour plots of the displacement field from DIC during the experimental test for the second buckling mode: (a) global displacement $\hat{u}$ of the central node at the reference configuration and at steps P_1^{bk2}, P_2^{bk2} and P_3^{bk2}; (b) local transversal displacement u_2 of bar 2 at step P_1^{bk2};(c) local displacement u_2 of bar 2 at step P_2^{bk2};(d) local displacement u_2 of bar 2 at step P_3^{bk2}.

that region.

The dashed black line in Figure 13b is obtained with an averaged linear regression of both experimental data, considering only those with $\hat{u} < 8.5$ mm. This curve represents the initial trend of Δu_2 in the compressed bar, which is due only to geometric imperfections. As previously mentioned, in the red region the growth rate of displacement increases and the experimental data deviate from the black line. From Figure 13c, we observe that right after P_1^{bk2} the data are affected by noise due to the change in deformation mode, but then they follow a trend with a higher stiffness. This trend reflects the bending stiffness of the deformed shape during buckling mode 2. After P_2^{bk2}, there is a sensible reduction of the stiffness and this indicates that Euler buckling associated to mode 2 is taking place.

The above discussion demonstrated that Euler instability occurs near points P_2^{bk1} and P_2^{bk2}. Therefore, from Figure 10 we observe that the predictions of analytical and FE models (green and blue circles) are very

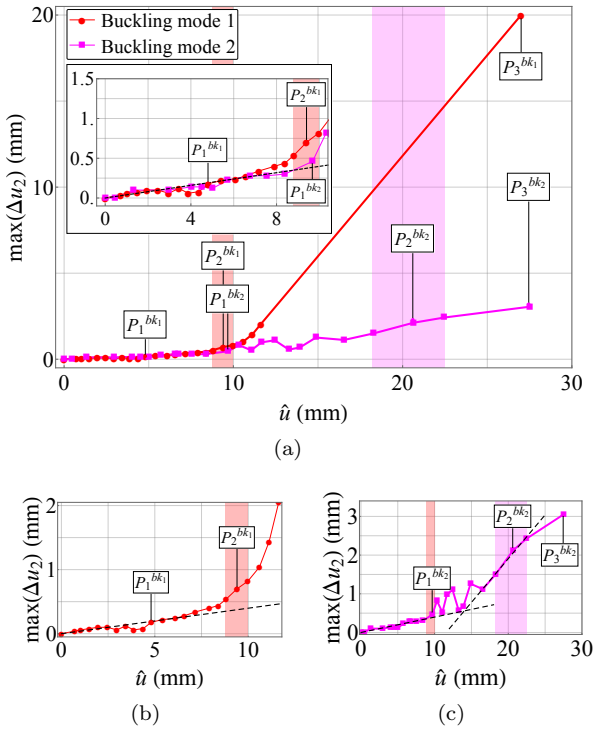

Figure 13: (a) Trend of the maximum values of the relative transversal displacement Δu_2 of bar 2 during the tests for first and second buckling modes, plotted as a function of displacement $\hat{u}$ of the central hinge. Red and magenta zones identify the regions where, respectively, first and second buckling modes are experimentally observed. The details of first and second buckling modes are shown separately in figures (b) and (c), respectively.

close to the experimental buckling points. This provides a validation of the analytical approach presented in Appendix A. We remark that the proposed analytical model gives a prediction of Euler buckling but does not describe the post-critical behavior. This would require a model in nonlinear elasticity that couples axial and bending regimes, which is not the scope of the present work.

7. Conclusions

The equilibrium of the von Mises truss subjected to a horizontal load was studied from analytical, numerical and experimental points of view. The analytical model was developed in the framework of finite elasticity considering hyperelastic and isotropic materials. The original contribution of the present work is the proposal of a new hyperelastic law, expressed by Eq. (14), which is capable of describing hardening. The advantage of the proposed law is that the equilibrium maintains a straightforward mathematical form and allows obtaining a closed-form solution even for compressible materials. It was shown that the proposed hyperelastic model describes accurately the experimental response of rubbers with hardening.

An experimental device able to reproduce a von Mises truss under horizontal load was presented. A FE

analysis was carried out in COMSOL. The models were developed in three-dimensional nonlinear elasticity. The comparison between analytical, numerical and experimental results demonstrated that the proposed analytical model is accurate and suitable for the behavior of rubbers under very large stretches.

A formulation for the prediction of the Euler buckling load in nonlinear elasticity was presented. Differently from the one proposed in Falope et al. (2021), the present formulation takes into account shear deformation. The comparison with experimental and FE results showed that the analytical prediction is accurate for both first and second buckling modes.

Acknowledgments

The authors gratefully acknowledge the financial support of the Italian Ministry of University and Research (MUR) through research grant PRIN 2020 No. 2020EBLPLS on "Opportunities and challenges of nanotechnology in advanced and green construction materials" and project FISR 2019 "Eco Earth" (code 00245). Financial support by the National Group of Mathematical Physics (GNFM-INdAM) is also acknowledged. The authors would like to thank Mr. Ivano Lanzoni, who built the experimental device according to the required technical specifications.

Appendix A. Analytical model for Euler buckling

Let us introduce the governing equation of a Timoshenko beam (Falope et al., 2020),

$$\left(1-\frac{P}{GA_r}\right)\varphi'''(z)+\frac{P}{EI_y}\varphi'(z)=0, \tag{A.1}$$

in which apex $'$ denotes differentiation with respect to the longitudinal variable z of the beam, $\varphi(z)$ is the rotation of the transversal cross section, P is the axial force, I_y the moment of inertia of the beam, A_r the shear area of the beam, and E and G the Young modulus and shear modulus, respectively. The derivative of transversal deflection of the beam, $v'(z)$, is defined as

$$v'(z)=\varphi''(z)\frac{1-\beta^2}{\alpha^2}-\varphi'(z), \tag{A.2}$$

being $\alpha=\sqrt{P/(EI_y)}$ and $\beta=\sqrt{1-P/(GA_r)}$. The solution of ordinary differential equations (A.1) and (A.2) provide the expressions of rotation and deflection of the beam, which read

$$\begin{aligned}\varphi(z)&=\frac{\beta}{\alpha}\left[c_1\sin\left(\frac{\alpha}{\beta}z\right)-c_2\cos\left(\frac{\alpha}{\beta}z\right)\right]+c_3,\\ v(z)&=\frac{1}{\alpha^2}\left[c_1\cos\left(\frac{\alpha z}{\beta}\right)+c_2\sin\left(\frac{\alpha z}{\beta}\right)\right]-c_3z+c_4,\end{aligned} \tag{A.3}$$

where c_i are unknown integration constants.

During the experiments on the von Mises truss (Figure 9) the compressed bar is clamped at its lower side and restrained with a sleeve at its upper side. Thus, the boundary conditions are $v(0) = v(L_m) = 0$ and $\varphi(0) = \varphi(L_m) = 0$. Using relations (A.3) we obtain the following system of equations:

$$\begin{bmatrix} 0 & -\frac{\beta}{\alpha} & 1 & 0 \\ \frac{\beta}{\alpha}\sin\left(\frac{\alpha L_m}{\beta}\right) & -\frac{\beta}{\alpha}\cos\left(\frac{\alpha L_m}{\beta}\right) & 1 & 0 \\ \frac{1}{\alpha^2} & 0 & 0 & 1 \\ \frac{1}{\alpha^2}\cos\left(\frac{\alpha L_m}{\beta}\right) & \frac{1}{\alpha^2}\sin\left(\frac{\alpha L_m}{\beta}\right) & -L_m & 1 \end{bmatrix} \begin{bmatrix} c_1 \\ c_2 \\ c_3 \\ c_4 \end{bmatrix} = \begin{bmatrix} 0 \\ 0 \\ 0 \\ 0 \end{bmatrix}. \tag{A.4}$$

The buckling loads of the bar are the eigenvalues of the coefficient matrix of Eq. (A.4), which are obtained as roots of the characteristic equation

$$\alpha\beta L_m \sin\left(\frac{\alpha L_m}{\beta}\right) + 2\cos\left(\frac{\alpha L_m}{\beta}\right) = 2. \tag{A.5}$$

Eq. (A.5) represents a transcendental equation that must be solved numerically. Note that this equation is reduced to the case of an Euler-Bernoulli beam model when $GA_r \to \infty$, namely $\beta = 1$ (Nayfeh & Emam, 2008; Emam & Lacarbonara, 2022).

In the classical linear buckling analysis, the geometric and mechanical properties of the beam are defined in undeformed configuration. However, in order to account for both geometric and constitutive nonlinearities, such quantities must be evaluated in deformed configuration. To do so, we introduce the length of the beam, the shear area and the moment of inertia as functions of the prescribed displacement $\hat{u}$, namely

$$A_r(\hat{u}) = \frac{5}{6} t\, h\, \lambda_2^2, \quad L_m(\hat{u}) = l_{m2}, \quad I_y(\hat{u}) = \frac{\lambda_2^4\, h\, t^3}{12}, \tag{A.6}$$

where l_{2m} and λ_2 are the deformed length and the transversal stretch of the compressed bar, defined respectively by Eqs. $(3)_2$ and (8). The constitutive nonlinearities are introduced by defining the tangent elastic moduli $E(\hat{u})$ and $G(\hat{u})$. The tangent Young modulus represents the variable slope of the nominal stress vs. longitudinal stretch law of bar 2 (Figure 5), computed as

$$E(\hat{u}) = \frac{1}{t\, h} \frac{\partial N_2}{\partial \lambda_{2,z}}, \tag{A.7}$$

where N_2 is defined in Eq. (9). The tangent shear modulus $G(\hat{u})$ is related to the tangent Young modulus

and Poisson ratio $\nu(\hat{u})$ as

$$G(\hat{u}) = \frac{1}{2}\frac{E(\hat{u})}{1+\nu(\hat{u})}, \tag{A.8}$$

in which $\nu(\hat{u})$ is defined as the ratio between traversal and longitudinal strains of the bar (Pelliciari & Tarantino, 2021), namely

$$\nu(\hat{u}) = \frac{1-\lambda_2}{\lambda_{2,z}-1}. \tag{A.9}$$

The expressions of terms α and β accounting for geometric and constitutive nonlinearities become

$$\alpha_n = \sqrt{\frac{P(\hat{u})}{E(\hat{u})I_y(\hat{u})}}, \quad \beta_n = \sqrt{1-\frac{P(\hat{u})}{G(\hat{u})A_r(\hat{u})}}. \tag{A.10}$$

Substitution of Eq. (A.10) into Eq. (A.5) gives the following characteristic equation:

$$\alpha_n\beta_n l_{m2}\sin\left(\frac{\alpha_n l_{m2}}{\beta_n}\right) + 2\cos\left(\frac{\alpha_n l_{m2}}{\beta_n}\right) = 2. \tag{A.11}$$

For a given value of $\hat{u}$, the buckling loads P_{bk} of the compressed bar are obtained from the numerical solution of Eq. (A.11).

We are now interested in the buckling loads of the von Mises truss when subjected to a horizontal load. Hence, we want to determine which configurations $(\hat{u}, \hat{w})$ of the equilibrium path of Figure 7 correspond to buckling of bar 2. To this aim, for each configuration of the von Mises truss, we define a virtual critical load path as the external horizontal force F_{bk} that causes buckling of bar 2. The critical load path is obtained from the equilibrium of control point C assuming $N_2 = P_{bk}$ [5]. The axial force N_1 of the bar under tension, expressed by Eq. (9), remains unchanged. This because the displacement components $(\hat{u}, \hat{w})$ are the ones of the equilibrium path in Figure 7. The new unknown variables of the equilibrium equations are the horizontal buckling force F_{bk} and the virtual vertical force $\tilde{F}_Z$. Force $\tilde{F}_Z$ is considered virtual because it is introduced for the sole purpose of ensuring equilibrium of node C during the critical load path. The equilibrium equations defining the critical load path are

$$\begin{cases} F_{bk} - N_1\cos\theta_1 + P_{bk}\cos\theta_2 = 0 \\ \tilde{F}_Z + N_1\sin\theta_1 + P_{bk}\sin\theta_2 = 0 \end{cases} \tag{A.12}$$

Buckling load P_{bk} of bar 2 is computed for each configuration $(\hat{u}, \hat{w})$ by solving Eq. (A.11).

Along the equilibrium path of the von Mises truss, buckling occurs if and only if the following three

[5] From now on the dependence on $\hat{u}$ and $\hat{w}$ will be omitted for sake of simplicity.

conditions are simultaneously fulfilled:

$$\begin{cases} F_{bk} = F \\ \tilde{F}_Z = 0 \\ N_2 < 0 \end{cases} \tag{A.13}$$

where F is the horizontal force obtained as solution of the equilibrium of the truss without buckling, expressed by Eq. (7). Eq.(A.13)$_1$ means that buckling occurs at the intersection between equilibrium path and critical buckling path. Eq.(A.13)$_2$ means that buckling occurs if and only if the virtual vertical force vanishes. This because such force is not present in the actual von Mises truss and therefore the only congruent configurations are those where $\tilde{F}_Z$ vanishes. Eq.(A.13)$_3$ states that, as it is obvious, buckling occurs only if bar 2 is subjected to compression.

Figure A.14a shows the equilibrium path of the truss and the critical buckling paths associated to buckling modes 1, 2 and 3, which are obtained by solving Eq. (A.12). We observe that each of the three critical paths have multiple intersections with the equilibrium path. However, the three conditions of Eq. (A.13) must be simultaneously checked and therefore a plot of both $\tilde{F}_Z$ and N_2 is given in Figure A.14b. From this plot we conclude that only the configurations identified by red and magenta dots fulfill all three conditions of Eq. (A.13). These configurations are thus the only ones where Euler buckling can be actually observed.

The two red dots correspond to the configurations where first and second buckling modes take place. The two magenta dots are configurations where first and second buckling modes could potentially be observed. However, when loading the truss, such modes already took place in earlier configurations (red dots) and thus they are not of interest. From now on we will thus discard such buckling points and focus only on the first buckling configurations where modes 1 and 2 occur.

The buckling configurations associated with first and second modes take place respectively at ($\hat{u}_{bk_1} = 9.13, \hat{w}_{bk_1} = 0.21$) mm and ($\hat{u}_{bk_2} = 21.52, \hat{w}_{bk_2} = 1.1$) mm. In such configurations, the two bars undergo longitudinal stretches ($\lambda_{1,z} = 1.04, \lambda_{2,z} = 0.95$) and ($\lambda_{1,z} = 1.12, \lambda_{2,z} = 0.91$).

The third mode does not take place because, as visible in Figure A.14b, it does not intersect the load path, namely it does not fulfil condition (A.13)$_1$. We will thus investigate only the first and second buckling modes. Note that the intersection between equilibrium path and critical path of mode 3 does not occur only because of a small gap. Therefore, to make sure that mode 3 does not take place in the FE model, four prismatic joints were inserted (see Section 4).

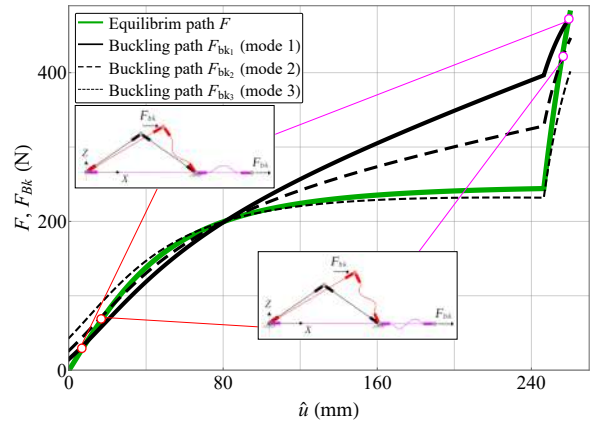

(a)

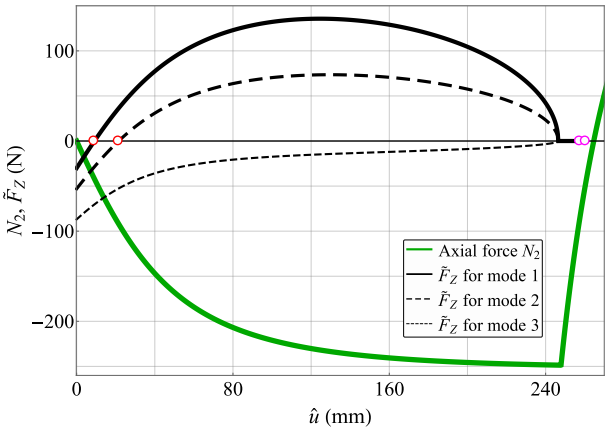

(b)

Figure A.14: Euler buckling analysis of the von Mises truss: (a) equilibrium path without buckling (green curve) and critical buckling paths associated with buckling modes 1, 2 and 3 (black curves); (b) axial force N_2 of the compressed bar (green curve) and virtual vertical forces $\tilde{F}_Z$ associated with buckling modes 1, 2 and 3 (black curves). Multiple intersections are found but only the configurations in red and magenta dots fulfill all three conditions of Eq. (A.13). Hence, only such points represent buckling configurations.

References

Barbarino, S., Gandhi, F. S., & Visdeloup, R. (2013). A bi-stable von-Mises truss for morphing applications actuated using shape memory alloys. In *Smart Materials, Adaptive Structures and Intelligent Systems* (p. V001T01A004). ASME volume 56031. doi:https://doi.org/10.1115/SMASIS2013-3062.

Bažant, Z. P., & Cedolin, L. (1991). *Stability of structures: elastic, inelastic, fracture and damage theories*. World Scientific.

Bazzucchi, F., Manuello, A., & Carpinteri, A. (2017). Interaction between snap-through and Eulerian instability in shallow structures. *International Journal of Non-Linear Mechanics*, *88*, 11–20. doi:https://doi.org/10.1016/j.ijnonlinmec.2016.10.006.

Bellini, P. X. (1972). The concept of snap-buckling illustrated by a simple model. *International Journal of Non-Linear Mechanics*, *7*, 643–650. doi:https://doi.org/10.1016/0020-7462(72)90004-2.

Borri, C., Majowiecki, M., & Spinelli, P. (1992). Wind response of a large tensile structure: The new roof of the olimpic stadium in Rome. *Journal of Wind Engineering and Industrial Aerodynamics*, *42*, 1435–1446.

Cai, J., Feng, J., & Xu, Y. (2019). Effects of elastic supports on the snap-through buckling of Mises trusses. *Mechanics of Solids*, *54*, 486–490.

Catbas, F. N., Susoy, M., & Frangopol, D. M. (2008). Structural health monitoring and reliability estimation: Long span truss bridge application with environmental monitoring data. *Engineering structures*, *30*, 2347–2359.

Chen, J. S., & Hung, S. Y. (2011). Snapping of an elastica under various loading mechanisms. *European Journal of Mechanics-A/Solids*, *30*, 525–531.

Chen, J. S., & Lee, C. C. (2021). Vibration and snapping of a self-contacted beam under prescribed end rotations. *European Journal of Mechanics-A/Solids*, *85*, 104128.

Chi, Y., Li, Y., Zhao, Y., Hong, Y., Tang, Y., & Yin, J. (2022). Bistable and multistable actuators for soft robots: Structures, materials, and functionalities. *Advanced Materials*, *34*, 2110384.

Ciarlet, P. G., & Geymonat, G. (1982). Sur les lois de comportement en élasticité non linéaire compressible. *C. R. Acad. Sci. Ser. II*, *295*, 423–426.

Emam, S., & Lacarbonara, W. (2022). A review on buckling and postbuckling of thin elastic beams. *European Journal of Mechanics-A/Solids*, *92*, 104449.

Falope, F. O., Lanzoni, L., & Radi, E. (2020). Buckling of a timoshenko beam bonded to an elastic half-plane: Effects of sharp and smooth beam edges. *International Journal of Solids and Structures*, *185*, 222–239.

Falope, F. O., Pelliciari, M., Lanzoni, L., & Tarantino, A. M. (2021). Snap-through and Eulerian buckling of the bi-stable von Mises truss in nonlinear elasticity: A theoretical, numerical and experimental investigation. *International Journal of Non-Linear Mechanics*, *134*, 103739.

Fenci, G. E., & Currie, N. G. R. (2017). Deployable structures classification: A review. *International Journal of Space Structures*, *32*, 112–130.

Ferrari, F., Sigmund, O., & Guest, J. K. (2021). Topology optimization with linearized buckling criteria in 250 lines of Matlab. *Structural and Multidisciplinary Optimization*, *63*, 3045–3066.

Fonseca, F. M., & Gonçalves, P. B. (2022). Nonlinear behavior and instabilities of a hyperelastic von Mises truss. *International Journal of Non-Linear Mechanics*, *142*, 103964.

Gent, A. (1996). A new constitutive relation for rubber. *Rubber Chem Technol*, *69*, 59–61.

Guo, X., Cheng, G. D., & Olhoff, N. (2005). Optimum design of truss topology under buckling constraints. *Structural and Multidisciplinary Optimization*, *30*, 169–180.

Haydar, H., Far, H., & Saleh, A. (2018). Portal steel trusses vs. portal steel frames for long-span industrial buildings. *Steel Construction*, *11*, 205–217.

Hill, R. (1979). Aspects of invariance in solid mechanics. *Advances in applied mechanics*, *18*, 1–75.

Horgan, C. O. (2015). The remarkable Gent constitutive model for hyperelastic materials. *International Journal of Non-Linear Mechanics*, *68*, 9–16.

Knowles, J. K. (1977). The finite anti-plane shear field near the tip of a crack for a class of incompressible elastic solids. *International Journal of Fracture*, *13*, 611–639.

Kwasniewski, L. (2009). Complete equilibrium paths for Mises trusses. *International Journal of Non-Linear Mechanics*, *44*, 19–26. doi:https://doi.org/10.1016/j.ijnonlinmec.2008.08.011.

Lanzoni, L., & Tarantino, A. M. (2015). Equilibrium configurations and stability of a damaged body under uniaxial tractions. *Zeitschrift für angewandte Mathematik und Physik*, *66*, 171–190. doi:https://doi.org/10.1007/s00033-014-0397-6.

Levin, S. M. (2002). The tensegrity-truss as a model for spine mechanics: biotensegrity. *Journal of mechanics in medicine and biology*, *2*, 375–388.

Ligaro, S. S., & Valvo, P. S. (2006). Large displacement analysis of elastic pyramidal trusses. *Int J Solids Struct*, *43*, 4867–4887.

Madah, H., & Amir, O. (2017). Truss optimization with buckling considerations using geometrically nonlinear beam modeling. *Computers & Structures*, *192*, 233–247.

Mises, R. V. (1923). Über die stabilitätsprobleme der elastizitätstheorie. *ZAMM-Journal of Applied Mathematics and Mechanics/Zeitschrift für Angewandte Mathematik und Mechanik*, *3*, 406–422. doi:https://doi.org/10.1002/zamm.19230030602.

Mulhern, J. L., Protzman, N. M., White, A. M., & Brigido, S. A. (2016). Salvage of failed total ankle replacement using a custom titanium truss. *The Journal of Foot and Ankle Surgery*, *55*, 868–873.

Nayfeh, A. H., & Emam, S. A. (2008). Exact solution and stability of postbuckling configurations of beams. *Nonlinear Dynamics*, *54*, 395–408.

Ogden, R. W. (1972). Large deformation isotropic elasticity: on the correlation of theory and experiment for compressible rubberlike solids. *Proc R Soc London, Ser A*, (pp. 567–583).

Orlando, D., de Castro, C. H. L., & Gonçalves, P. B. (2018). Nonlinear vibrations and instability of a bistable shallow reticulated truss. *Nonlinear Dynamics*, *94*, 1479–1499. doi:https://doi.org/10.1007/s11071-018-4437-1.

Parthasarathy, J., Starly, B., & Raman, S. (2011). A design for the additive manufacture of functionally graded porous structures with tailored mechanical properties for biomedical applications. *Journal of Manufacturing Processes*, *13*, 160–170.

Paulose, J., Meeussen, A. S., & Vitelli, V. (2015). Selective buckling via states of self-stress in topological metamaterials. *Proceedings of the National Academy of Sciences*, *112*, 7639–7644. doi:https://doi.org/10.1073/pnas.1502939112.

Pecknold, D. A., Ghaboussi, J., & Healey, T. J. (1985). Snap-through and bifurcation in a simple structure. *Journal of Engineering Mechanics*, *111*, 909–922. doi:https://doi.org/10.1061/(ASCE)0733-9399(1985)111:7(909).

Pelliciari, M., & Tarantino, A. M. (2020a). Equilibrium paths for von Mises trusses in finite elasticity. *Journal of Elasticity*, *138*, 145–168. doi:https://doi.org/10.1007/s10659-019-09731-1.

Pelliciari, M., & Tarantino, A. M. (2020b). Equilibrium paths of a three-bar truss in finite elasticity with an application to graphene. *Mathematics and Mechanics of Solids*, *25*, 705–726. doi:https://doi.org/10.1177/1081286519887470.

Pelliciari, M., & Tarantino, A. M. (2021). Equilibrium and stability of anisotropic hyperelastic graphene membranes. *Journal of Elasticity*, *144*, 169–195.

Schioler, T., & Pellegrino, S. (2007). Space frames with multiple stable configurations. *AIAA journal*, *45*, 1740–1747. doi:https://doi.org/10.2514/1.16825.

Schorr, P., Böhm, V., Zentner, L., & Zimmermann, K. (2018). Motion characteristics of a vibration driven mobile tensegrity structure with multiple stable equilibrium states. *Journal of Sound and Vibration*, *437*, 198–208. doi:https://doi.org/10.1016/j.jsv.2018.09.019.

Silva, W. T. M., Nascimento, É. L. R., & Bezerra, L. M. (2021). Analytical and numerical approach to detect limit and bifurcation points of Mises truss with out-of-plane lateral linear spring. *Journal of Engineering Mechanics*, *147*, 04021018.

Wu, M., Zhang, W., & Niu, Y. (2021). Experimental and numerical studies on nonlinear vibrations and dynamic snap-through phenomena of bistable asymmetric composite laminated shallow shell under center foundation excitation. *European Journal of Mechanics-A/Solids*, *89*, 104303.

Zhang, R., Guo, X., Liu, Y., & Leng, J. (2014). Theoretical analysis and experiments of a space deployable truss structure. *Composite structures*, *112*, 226–230.

Zhang, Y., Tichem, M., & van Keulen, F. (2021). Rotational snap-through behavior of multi-stable beam-type metastructures. *International Journal of Mechanical Sciences*, *193*, 106172. doi:https://doi.org/10.1016/j.ijmecsci.2020.106172.

Ziegler, H. (2013). *Principles of structural stability* volume 35. Birkhäuser.